JBC RESEARCH ARTICLE

The *Pyrococcus furiosus* ironome is dominated by $[Fe_4S_4]^{2+}$ clusters or thioferrate-like iron depending on the availability of elemental sulfur

Received for publication, February 21, 2021, and in revised form, April 12, 2021 Published, Papers in Press, April 28, 2021,
https://doi.org/10.1016/j.jbc.2021.100710

Shaik Waseem Vali[1], Dominik K. Haja[2], Richard A. Brand[3,4], Michael W. W. Adams[2], and Paul A. Lindahl[1,5,*]

From the [1]Department of Biochemistry and Biophysics, Texas A&M University, College Station, Texas, USA; [2]Department of Biochemistry and Molecular Biology, University of Georgia, Athens, Georgia, USA; [3]Faculty of Physics, University of Duisburg-Essen, Duisburg, Germany; [4]Institute of Nanotechnology, Karlsruhe Institute of Technology, Eggenstein-Leopoldshafen, Germany; [5]Department of Chemistry, Texas A&M University, College Station, Texas, USA

Edited by F. Peter Guengerich

Pyrococcus furiosus **is a hyperthermophilic anaerobic archaeon whose metabolism depends on whether elemental sulfur is (+S^0) or is not (-S^0) included in growth medium. Under +S^0 conditions, expression of respiratory hydrogenase declines while respiratory membrane-bound sulfane reductase and the putative iron-storage protein IssA increase. Our objective was to investigate the iron content of WT and ΔIssA cells under these growth conditions using Mössbauer spectroscopy. WT-S^0 cells contained ∼1 mM Fe, with ∼85% present as two spectroscopically distinct forms of S = 0 $[Fe_4S_4]^{2+}$ clusters; the remainder was mainly high-spin Fe^{II}. WT+S^0 cells contained 5 to 9 mM Fe, with 75 to 90% present as magnetically ordered thioferrate-like (TFL) iron nanoparticles. TFL iron was similar to chemically defined thioferrates; both consisted of Fe^{III} ions coordinated by an S_4 environment, and both exhibited strong coupling between particles causing high applied fields to have little spectral effect. At high temperatures with magnetic hyperfine interactions abolished, TFL iron exhibited two doublets overlapping those of $[Fe_4S_4]^{2+}$ clusters in -S^0 cells. This coincidence arose because of similar coordination environments of TFL iron and cluster iron. The TFL structure was more heterogeneous in the presence of IssA. Presented data suggest that IssA may coordinate insoluble iron sulfides as TFL iron, formed as a byproduct of anaerobic sulfur respiration under high iron conditions, which thereby reduces its toxicity to the cell. This was the first Mössbauer characterization of the ironome of an archaeon, and it illustrates differences relative to the iron content of better-studied bacteria such as *Escherichia coli*.**

Pyrococcus furiosus is a hyperthermophilic anaerobic archaeon that grows near marine volcanic vents at temperatures approaching 100 °C (1). These cells grow on carbohydrates or peptides and produce acetate, CO_2, and either H_2 or H_2S depending on whether elemental sulfur (S^0) is included in the growth medium. The iron concentration in the organism is high; this d-block transition metal plays critical roles in the cell's metabolism, especially in processes involving redox and energy generation (2). Bioinformatic analysis predicts that there are 178 iron-containing proteins (Table S1) (3), 27 of which have been purified (Table S2); at least 15 of those purified contain $[Fe_4S_4]$ clusters. This represents 8.4% of the *P. furiosus* genome, which is slightly above average for archaea (7.1%) and well above average for bacteria (3.9%) and eukaryotes (1.1%) (4, 5).

During peptide fermentation, homodimeric aldehyde ferredoxin oxidoreductase (AOR) oxidizes aldehydes derived from amino acids. Each AOR subunit contains an $[Fe_4S_4]$ cluster. Bridging the subunits of the homodimer is a monomeric Fe ion coordinated by His and Glu residues (6). AOR constitutes ∼1% of the total protein in the cell (7). Formaldehyde ferredoxin oxidoreductase, pyruvate ferredoxin oxidoreductase, 2-ketoisovalerate ferredoxin oxidoreductase, 2-ketoglutarate ferredoxin oxidoreductase, and indolepyruvate ferredoxin oxidoreductase are all $[Fe_4S_4]$ cluster-containing enzymes that catalyze catabolic processes. The latter enzymes catalyze the oxidative decarboxylation of 2-keto acids derived from peptides (8–10). Electrons from these catabolic metalloenzymes reduce a monomeric ferredoxin that houses a single $[Fe_4S_4]^{2+/1+}$ cluster ($E^{0'}$ ∼ −480 mV *versus* NHE) coordinated by three Cys and one Asp residues.

Carbohydrate fermentation involves a modified Embden-Meyerhof pathway that is independent of NAD. Glyceraldehyde-3-phosphate ferredoxin oxidoreductase, another $[Fe_4S_4]$-containing enzyme, oxidizes glyceraldehyde-3-phosphate to glycerate-3-phosphate, and transfers the electrons obtained to the ferredoxin.

Ferredoxin not only receives electrons but it donates them as part of energy generation in the cell; thus, it serves as the electron *currency* for the cell. An evolutionarily ancient membrane-bound respiratory hydrogenase (MBH) is used to oxidize ferredoxin (11). This contains at least three $[Fe_4S_4]$ clusters and a NiFe active-site cluster. Ferredoxin donates electrons to MBH which transfers them, in turn, to protons ($E^{0'}$ = −420 mV at pH 7), forming H_2 as the product. This thermodynamically favorable redox process pumps H^+ ions

* For correspondence: Paul A. Lindahl, lindahl@chem.tamu.edu.

across the membrane, which are then exchanged with Na^+ ions. This creates a concentration gradient that is used by a Na^+-dependent ATP synthase to generate ATP *via* chemiosmosis. Ferredoxin also donates electrons to NADH-dependent reduced ferredoxin:$NADP^+$ oxidoreductase 1 which reduces $NADP^+$ in an electron bifurcation reaction that generates low-potential electrons which can be used in metabolic processes requiring low potentials.

Carbohydrate fermentation can occur with or without S^0, whereas cells grown on peptides require S^0 as there is little growth when it is omitted from the growth medium (12). The metabolism of *P. furiosus* changes significantly when elemental sulfur (S^0) is included in the growth medium (13). Under $+S^0$ conditions, *P. furiosus* shuts-down expression of MBH and of the two NAD(P)-reducing soluble hydrogenases termed SHI and SHII (among other proteins) and upregulates expression of a membrane-bound sulfane reductase (MBS) (Tables S3 and S4, (14)). Doing so suppresses production of H_2 and stimulates H_2S production. MBS uses electrons from ferredoxin to reduce sulfane sulfurs of polysulfides ($E^{0'}$ = −260 mV), generating smaller polysulfide units as illustrated by the following sample reaction.

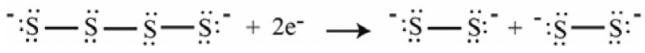

MBS cleaves organic and anionic polysulfides but not to the level of H_2S, which is formed spontaneously from smaller polysulfides (S_n^{2-} where n ≤ 4). Like MBH, MBS creates a Na^+ ion gradient which is subsequently used, *via* chemiosmosis, for ATP synthesis. MBS is a homolog of MBH and also contains three [Fe_4S_4] clusters. Unlike MBH, it does not contain a NiFe active site (15).

The S^0-dependent shift in metabolism is controlled by transcription factor SurR (16, 17). Under $+S^0$ conditions, SurR upregulates iron transport and iron sulfur cluster (ISC) biosynthesis genes. *P. furiosus* grows better with S° than without it; in fact, the maximal yield (cell mass produced per mole of carbohydrate used) is nearly double that obtained under $-S^0$ conditions. This implies that more energy can be generated by coupling ferredoxin oxidation to S° reduction than by coupling it to proton reduction, a conclusion substantiated by the finding that MBS contains an additional ion pump compared with MBH (15).

Despite being an anaerobe, *P. furiosus* houses iron-containing proteins that protect it against damage because of reactive oxygen species (ROS). Superoxide reductase catalyzes the reduction of superoxide to H_2O_2 at an active site containing a single Fe^{II} ion. The electrons required for this come from rubredoxin, a protein that houses a mononuclear redox-active Fe^{II}/Fe^{III} ion coordinated by four cysteine residues in a tetrahedral geometry – an $Fe^{II/III}(S)_4$ site (18). Rubrerythrin catalyzes the reduction of H_2O_2 to water, also using electrons from rubredoxin. It contains an [Fe-O-Fe] center as well as an $Fe^{II/III}(S)_4$ site (19).

P. furiosus contains at least two proteins that store iron, including ferritin and a "miniferritin" DPS-like protein. Ferritin stores thousands of ferric ions within the core of a 24-subunit protein complex as an insoluble Fe^{III} ferrihydrite-type aggregate. The DPS-like protein has a ferroxidase active site ([Fe-O-Fe]) which exhibits peroxidase activity in the presence of H_2O_2. This protein coordinates hundreds of iron ions, obtained from the H_2O_2-dependent oxidation of Fe^{II} (20, 21).

Another protein that binds a large amount of iron is IssA. The exact function of the IssA protein is unknown but its expression increases dramatically when cells are grown in $+S^0$ media, but only when iron is present (>7.4 μM) (22). Vaccaro *et al.* (23) suggested that IssA stores iron as thioferrates in which Fe^{III} and S^{2-} ions form anionic chains of edge-sharing FeS_4 tetrahedra that are charge-neutralized by cations such as Na^+ or K^+. Using TEM, they detected iron-dense particles 20 to 300 nm in diameter in $+S^0$ *P. furiosus* cells (23). X-ray absorption spectra of the particles indicate a linear polymeric $(FeS_2^-)_n$ structure as in thioferrates; this includes four Fe-S interactions at 2.24 Å, two Fe-Fe interactions at 2.70 Å, and a long-range Fe-Fe interaction at 5.4 Å. The particles exhibit a broad isotropic electron paramagnetic resonance (EPR) signal at g = 2.2 that displays anti-Curie Law behavior, also consistent with thioferrates. The EPR signal is observed only above 60 K, similar to the behavior of synthetic thioferrates. Moreover, the iron and sulfur from IssA-associated particles assemble into [Fe_4S_4] clusters. Such clusters can transfer to apo-ferredoxin (in the presence of DTT), indicating that these thioferrate particles can be used in ISC assembly. Purified IssA monomers reportedly contain 38 Fe and 38 S atoms. A 20 nm diameter 3.5 MDa thioferrate structure is calculated to contain ∼6400 Fe atoms and ∼170 IssA monomers. IssA contains only one cysteine per monomer raising issues as to how it coordinates such structures.

In this study, we have used primarily Mössbauer (MB) spectroscopy to analyze the iron content of ^{57}Fe-enriched WT and ΔIssA whole *P. furiosus* cells grown on the disaccharide maltose in the presence ($+S^0$) and absence ($-S^0$) of elemental sulfur. All ^{57}Fe ions in a sample are detectable by MB spectroscopy, with intensities that are roughly invariant per iron in the sample, regardless of the type of iron center. Thus, MB can be used to evaluate the ironome of these cells, albeit in semiquantitative terms and only with "coarse-grain" resolution. Using this approach, we have previously evaluated the ironome of *Escherichia coli* (24), *Saccharomyces cerevisiae* (25), and human Jurkat cells (26). This is the first MB study of an archaeon, in this case one that is hyperthermophilic and strictly anaerobic.

Results

WT-S^0 cells harvested while growing exponentially

We began by collecting low-temperature low-field MB spectra of whole WT cells harvested while growing exponentially on maltose with 10 μM ^{57}Fe and without S^0 in the medium. The 5 K 0.05 T MB spectrum was dominated by a broad quadrupole doublet representing ca. 85% of the overall intensity (Fig. 1*A*). The structured lineshape of the doublet

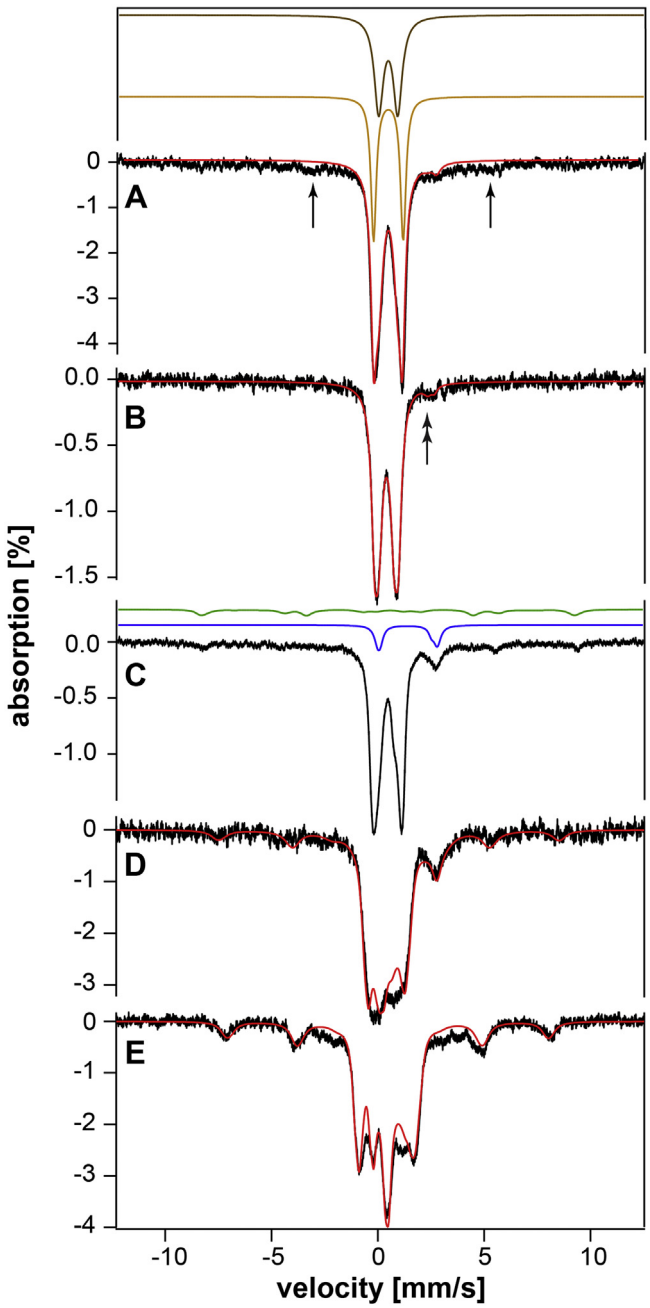

Figure 1. Mössbauer spectra of WT *P. furiosus* cells grown under -S^0 conditions and harvested during exponential growth. *A*, 5 K, 0.05 T; *B*, 150 K, 0.05 T; *C*, 4.2 K, 0 T; *D*, 4.2 K, 3.0 T; and *E*, 4.2 K, 6.0 T. The field was applied parallel (*A* and *B*) and perpendicular (*C–E*) to the gamma radiation.

prompted us to decompose it into two partially resolved sharper doublets, each with isomer shifts δ typical of oxidized S = 0 $[Fe_4S_4]^{2+}$ clusters (Table 1). The doublets were simulated by the gold and brown solid lines of Figure 1. The quadrupole splitting ΔE_Q associated with the gold doublet was wider than that of the brown doublet, and so we labeled them *wide* and *narrow* ISC *doublets* (ISC_W and ISC_N). Each doublet represented 35% to 45% of spectral intensity; the exact percentage due to each was difficult to assess because they were not well resolved. Considering that the spectrum represented *all* irons in the cell, including at least 15 different $[Fe_4S_4]$-containing proteins (Table S2), the ability to decompose all $[Fe_4S_4]$ clusters into two doublets, each with relatively sharp linewidths, was remarkable. One extreme explanation was that two of the 15 $[Fe_4S_4]$-containing proteins in the cell dominated the iron content of the cell, with each protein corresponding to the two doublets. At the other extreme, each $[Fe_4S_4]$-containing proteins in the cell might have contributed equally to the spectrum but, for some unknown reason, segregated cleanly into these two spectral groups. Neither extreme seems likely but they illustrate the remarkability of the result.

Also remarkable was that δ and ΔE_Q for the two doublets were strongly temperature-dependent. At 150 K (Fig. 1*B*), ΔE_Q and δ for both doublets declined (Table 1), but their linewidths did not increase. The temperature dependence of δ is mostly related to the second-order Doppler effect (27). The temperature-dependence of ΔE_Q is generally attributed to changes in the covalency of metal-ligand bonds. This can bring the separation between t_{2g} and e_g atomic orbitals close enough together that orbital populations can be affected by temperature, changing ΔE_Q.

Continuing with the extreme explanations offered above, this result would mean either that both dominant $[Fe_4S_4]$ proteins exhibited this behavior or that all 15 contributing $[Fe_4S_4]$ proteins did so. This raises an intriguing speculation that $[Fe_4S_4]^{2+}$ clusters in hyperthermophilic organisms might generally possess low-lying excited states.

We wanted to determine whether these doublets arose from diamagnetic iron centers, as would be the case if they arose from $[Fe_4S_4]^{2+}$ clusters. Spectra were collected at 4.2 K and 0, 3, and 6 T applied magnetic fields (Fig. 1, *C–E*). The solid red lines overlaying the data were simulations that assumed diamagnetism and the δ and ΔE_Q values in Table 1. The reasonable fits demonstrated that the $ISC_{W/N}$ doublets indeed arose from S = 0 $[Fe_4S_4]^{2+}$ clusters. This conclusion was reinforced by the large number of $[Fe_4S_4]$-containing proteins in these cell (Table S2). These spectra also show that virtually all redox-active $[Fe_4S_4]$ clusters in exponentially growing WT-S^0 cells are in the *oxidized* 2+ core state. $[Fe_4S_4]^{2+/1+}$ clusters typically have reduction potentials of ca. −400 mV *versus* NHE, suggesting (by considering the Nernst equation) a cellular potential >ca. −340 mV.

After MB spectra were collected, the sample was thawed, and after EPR analysis (see below), the metal content was determined (Table S5). We assumed that 70% of the sample volume in the packed MB cup was due to the cells themselves and that the density of the sample was 1.00 g/ml. With these assumptions, we calculated that the sample contained 1.03 mM iron. If two $[Fe_4S_4]$-containing proteins dominated this group, their cellular protein concentrations would be ∼120 μM each. On the other hand, if all 15 $[Fe_4S_4]$ proteins contributed equally, their the average cellular concentration would be ∼17 μM, which seems more likely.

WT-S^0 cells exhibited broad unresolved intensity barely distinguishable from the baseline between ca. −5 and +6 mm/s (Fig. 1*A*, arrows). This feature represented roughly 15% of the overall intensity and appeared to arise from a paramagnetic iron center. We overlaid the S^0-

Table 1
Mössbauer parameters used in simulations (averaged), LT (low temperature), and HT (high temperature)

Parameter	ISC_W	ISC_N	Magnetic	$Fe^{II}(S_4)$	$Fe^{II}(O/N)$	S = 5/2 Fe^{III}
δ (mm/s)	0.45 ± 0.04 (LT) 0.43 ± 0.03 (HT)	0.43 ± 0.03 (LT) 0.38 ± 0.05 (HT)		0.65 ± 0.04	1.3 ± 0.1 (LT) 1.2 ± 0.1 (HT)	0.50 ± 0.02
ΔE_Q (mm/s)	1.35 ± 0.05 (LT) 1.15 ± 0.1 (HT)	0.83 ± 0.06 (LT) 0.75 ± 0.07 (HT)		3.0 ± 0.05	2.6 ± 0.1 (LT) 2.7 ± 0.1 (HT)	0.45 ± 0.02
Γ (mm/s)	0.34 ± 0.06 (LT) 0.35 ± 0.05 (HT)	0.47 ± 0.04 (LT) 0.45 ± 0.04 (HT)		0.43 ± 0.03	0.5 ± 0.1 (LT) 0.5 ± 0.1 (HT)	0.50 ± 0.05
D; E/D						0.5; 0.33
A_x; A_y; A_z						−29.08 MHz
η						2.5 ± 0.5
g_x, g_y, g_z						2.0
Figure 1	45% (LT) 35% (HT) 43% (Post storage)	35% (LT) 60% (HT) 33% (Post storage)	∼14-15% (LT) (other)		4–5% (LT) 4–5% (HT) 8% (Post storage)	16% (Post storage)
Figure 3	10% (LT) 33% (HT)	10% (LT) 65% (HT)	78% (LT) (S°-dependent)		2% (LT) 2% (HT)	
Figure 6	+S°					
	10% (LT) 35% (LT)	10% (LT) 63% (HT)	77% (LT) (S°-dependent)		3% (LT) 3% (LT)	
	-S°					
	52% (LT) 42% (HT)	23% (LT) 33% (HT)		2% (LT) 2% (HT)	23% (LT) 23% (HT)	
Figure 7	49% (5 K) 44% (150 K)	36% (5 K) 41% (150 K)		3% (LT) 3% (HT)	12% (5 K) 12% (150 K)	

dependent thioferrate-like (TFL) magnetic material described below onto it, but the mismatch suggested a different type of magnetic iron (called "other magnetic iron" in Table 1). By 150 K, the associated magnetic hyperfine interactions collapsed completely into the spectral region occupied by the $ISC_{W/N}$ doublets (Fig. 1*B*). Importantly, we are not concluding that the absorption necessarily collapsed *into* the $ISC_{W/N}$ doublets at high temperature, only that it occupied/overlapped the same spectral region; more on this distinction below.

A small amount of a high-spin Fe^{II} doublet (∼5%) was also evident in the 150 K spectrum of WT-S^0 cells (Fig. 1*B*, double arrow). A similar doublet was probably present in the 5 K spectrum (Fig. 1*A*), but it could not be distinguished from the "other magnetic" iron. The parameters associated with this doublet are typical of mononuclear and binuclear Fe^{II} sites in proteins with 5 to 6 O/N donor atoms (Table S2), as well as any low-molecular-mass Fe^{II} species with a similar ligand environment. There are few if any sulfur donors in the $Fe^{II}(O/N)_{5–6}$ sites. Given the overall iron concentration in the cell, this doublet represented ∼50 μM $Fe^{II}(O/N)_{5–6}$ total in *P. furiosus* cells.

The 4.2 K 0 T spectrum of WT-S^0 cells in Figure 1*C* exhibited two minor features. One was a line at ∼2.6 mm/s which reflected an $Fe^{II}(O/N)_{5–6}$ doublet. This doublet was simulated by the blue solid line above the spectrum at 15% intensity. The broad nonsymmetrical shape of the high-energy line suggested at least two $Fe^{II}(O/N)_{5–6}$ sites. The second minor feature, simulated by the solid green line, was a pattern barely distinguishable from the baseline that suggested a high-spin Fe^{III} species. The putative S = 5/2 species was most evident at 6 T (Fig. 1*E*) where it represented ∼15% of overall spectral intensity.

The EPR spectrum of the sample (after thawing the MB sample and transferring it to an EPR tube) exhibited a signal at g = 4.3 which probably originated from the same species (Fig. 2, bottom). It also exhibited an isotropic signal at g = 2.00 but little intensity at g = 1.94 which is consistent with MB spectra showing that the $[Fe_4S_4]$ clusters in the cell were primarily in the diamagnetic 2+ core oxidation state.

The most surprising aspect of the Figure 1*C* spectrum was that the sample used to generate it was identical to that of Figure 1, *A* and *B*—only that it had been stored without thawing in a liquid N_2 dewar for ∼3 months. Because the $ISC_{W/N}$ doublets were unaffected, iron species other that the clusters affording the $ISC_{W/N}$ doublets (perhaps the "other magnetic" iron) must have reacted slowly in frozen cells to generate the observed high-spin Fe^{II} and Fe^{III} spectral features in Figure 1, *C–E*. The S = 5/2 Fe^{III} feature is probably an artefact as we have not observed similar features in other spectra. In contrast, $Fe^{II}(O/N)_{5–6}$ features were often observed under various conditions, and thus are likely physiologically relevant.

WT+S^0 cells harvested while growing exponentially

Another batch of *P. furiosus* cells was grown in the same medium except under +S^0 conditions. They were also harvested while growing exponentially. The low-temperature low-field MB spectrum of the WT+S^0 cells (Fig. 3*A*) was dominated by broad absorption that extended from ca. −6 mm/s to +7 mm/s velocity. Given previous studies showing large quantities of TFL material in +S^0 cells, we assigned it to this material. Consistent with that assignment, the EPR spectrum of cells in this state lacked a significant g = 4.3 signal (Fig. 2, top spectrum), indicating the absence of magnetically isolated high-spin S = 5/2 Fe^{III} paramagnetic material in the sample.

The spectrum exhibited two strong absorption lines in the same region of the $ISC_{W/N}$ doublets in WT-S^0 spectra, and this unfortunately created ambiguity for our analysis. It implies that some proportion of the intensity of these two lines arose from the $ISC_{W/N}$ doublets, whereas the remainder was associated with the TFL material. Based on our simulations and analyses, we estimate that at least 10%, and no more than 25% of the spectral intensity arose from the $ISC_{W/N}$ doublets

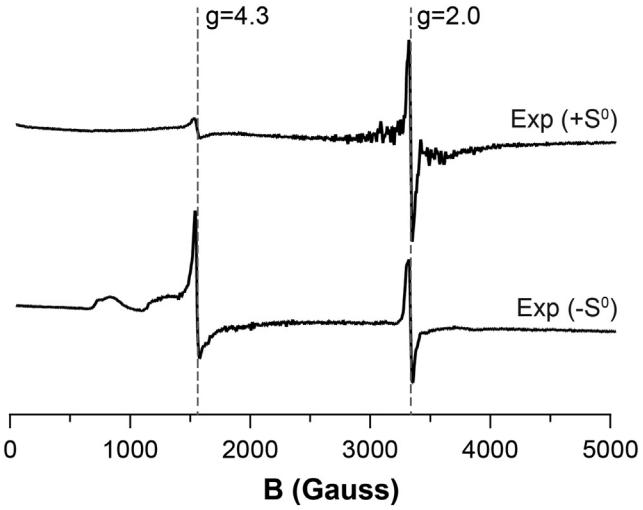

Figure 2. EPR spectra of WT cells grown under different sulfur conditions. *Top*, +S^0; Bottom, -S^0. EPR conditions: T, 4 K; frequency, 9.36 GHz; microwave power, 0.2 mW; modulation amplitude 10 G; modulation frequency 100 KHz; sweep time 300 s. +S^0, growth that includes elemental sulfur; -S^0, growth that excludes elemental sulfur; EPR, electron paramagnetic resonance.

in WT+S^0 spectra. The relative intensity of the two contributions was kept constant in the 3.0 and 6.0 T spectra (Fig. 3, *C* and *D*) with 20% of the intensity attributed to the $ISC_{W/N}$ doublets in the 6.0 T spectrum. The solid green lines in Figure 3, *A*, *C*, and *D* simulated the $ISC_{W/N}$ doublets at the 20% intensity level.

Magnetic hyperfine interactions associated with the TFL material were absent in the WT+S^0 spectrum at 150 K (Fig. 3*B*), and the intensity associated with this material collapsed into the same region that was occupied by the $ISC_{W/N}$ doublets in WT-S^0 spectra. The intensity of the ISC_W doublet increased from ∼10% at 5 K to 33% at 150 K. The intensity of ISC_N increased from ∼10% at 5 K to 65% at 150 K. Thus, 30% of the TFL material collapsed over the ISC_W doublet while 70% collapsed over the ISC_N doublet. None of the TFL material collapsed into features characteristic of Fe^{II} ions.

The 150 K MB spectrum of the WT+S^0 sample did exhibit a minor broad $Fe^{II}(O/N)_{5-6}$ doublet, representing ∼4% of spectral intensity (Fig. 3*B*, arrow). This doublet required two species for fitting, using parameters of mononuclear Fe^{II} species coordinated by 5 to 6 O/N and few if any S ligands (Table 1). These $Fe^{II}(O/N)_{5-6}$ sites are independent of the TFL material but became apparent once the hyperfine interactions associated with the TFL material collapsed.

We were initially surprised that the TFL magnetic material in WT+S^0 cells had isomer shift and quadrupole splitting parameters (56% δ = 0.37 mm/s and ΔE_Q = 0.75 mm/s; 44% δ =

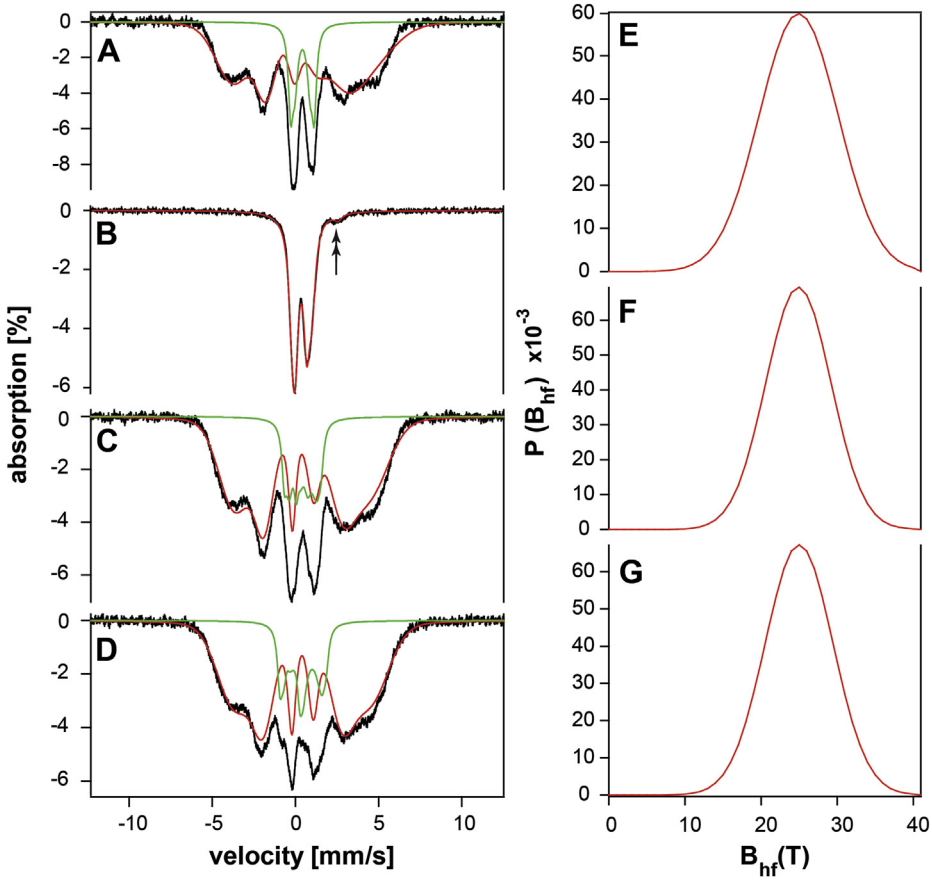

Figure 3. Mössbauer spectra of the WT+S^0 sample grown with 10 μM ^{57}Fe and S^0 in the medium, and harvested during exponential phase. *A*, 5 K 0.05 T; *B*, 150 K and 0.05 T; *C*, 4.2 K and 3 T; *D*, 4.2 K and 6.0 T. The applied magnetic field was perpendicular to the gamma radiation. The *red lines* in *A*, *C*, and *D* are simulations of the magnetically ordered iron using the continuous distribution of hyperfine fields in *E* (0.05 T), *F* (3 T), and *G* (6 T). *Green solid lines* are simulations to ISC_W and ISC_N contributions assuming 20% spectral intensity. +S^0, growth that includes elemental sulfur; -S^0, growth that excludes elemental sulfur.

0.42 mm/s and ΔE_Q = 1.15 mm/s) that were indistinguishable from those due to the S = 0 $[Fe_4S_4]^{2+}$ clusters in the WT-S^0 cells, given that the low-temperature magnetic properties of the two types of iron species were entirely different. This coincidence probably arose because the local structures of the two types of iron species were remarkably similar. Authentic sodium thioferrate ($NaFeS_2$) exhibits δ = 0.36 mm/s and ΔE_Q = 0.58 mm/s (28), which are similar to those of the TFL material *AND* $[Fe_4S_4]^{2+}$ clusters in these cells. Thioferrates consist of anionic linear chains of $((Fe^{III}S_2)^-)_n$ units, with each Fe^{III} ion coordinated by a tetrahedral environment of sulfide ligands with Na^+ or K^+ counter ions. Likewise, each iron of $[Fe_4S_4]$ clusters are locally coordinated by four sulfur ligands in a tetrahedral environment. The average formal oxidation state of iron in $[Fe_4S_4]^{2+}$ clusters is +2.5, with one delocalized electron shared by two irons in a "mixed-valence" $[Fe^{II}\ Fe^{III}]$ pair (the two pairs of a cluster are then antiferromagnetically coupled to generate the S = 0 system spin). There were clearly no localized $Fe^{II}(S)_4$ sites with sulfur donor sites in the TFL material, because otherwise an intense quadrupole doublet with δ ~0.7 mm/s and ΔE_Q ~3 mm/s (similar to reduced rubredoxin) would have been observed in the 150 K spectrum of Figure 3*B*. On the other hand, some *delocalized* $[Fe^{II}\ Fe^{III}]$ units might have contributed to the TFL structure.

We had hoped that high-field spectra of the WT+S^0 sample would have been sufficient to break the magnetic coupling responsible for the broadness and poor resolution of the magnetic material in low fields, but this was not observed. The spectra at 4.2 K and 0, 3, and 6 T perpendicular applied fields included contributions from both the magnetically ordered iron and ISCs (Fig. 3, *A*, *C* and *D*). The ISC contribution was calculated as described in Experimental procedures. The known external field and isomer shift were used to calculate the ISC portion of the spectrum so that in the fitting interaction only the area of this contribution was varied.

Technical details regarding the physical properties of the TFL material in WT+S^0 cells

The following technical aspects can be skipped without losing the major conclusion that the thioferrates-like material is similar to authentic thioferrates but with some subtle differences. This section provides details of those differences.

The magnetic part of the spectra (Fig. 3, *A*, *C* and *D* in red) was modeled with a histogram of hyperfine sextets over a range of effective hyperfine fields in steps of 1 T. The resulting histograms are presented in Figure 3, *E*–*G*. Small variations in δ and quadrupole line shift 2ε have been used to approximate the spectral asymmetry of the magnetic part. 2ε is similar to ΔE_Q, but it includes an angular dependence, even when the general asymmetry parameter η is absent in ΔE_Q, namely η = 0 (27).

These parameters were assumed linear in the effective hyperfine field over the fitted range. The intensities of each sextet were then used to calculate the distribution $P(B_{hf})$. The angle Θ of the hyperfine field B_{hf} with respect to the gamma radiation determines the line intensity ratio A_{23} between line pair 2 and 5 (nuclear transition with Δm = 0) to 3 and 4 (transitions with Δm = ± 1), which can vary between 0 (for Θ = 0; moments parallel to the gamma ray) and 4 (for Θ = 90°) according to the equation

$$A_{23} = \frac{4\sin^2\Theta}{1+\cos^2\Theta}$$

(27). An isotropic distribution of directions yields a ratio of 2, similar to what was observed (Fig. 4). In these experiments, the external magnetic field was perpendicular to the gamma rays. Thus, we can assume rotational symmetry around the field but not around the gamma ray direction. Useful relations for simple cases of magnetic texture have been described (29, 30).

Several changes are expected when a magnetic field is applied to a magnetically ordered system. First, for a ferromagnet or ferrimagnet, the magnetic moments should align parallel to the field. An antiferromagnet will align perpendicular to the field as long as the crystalline anisotropy is not too large. Because the orbital component of the Fe^{III} ions moments is zero (with the ground state configuration $[Ar]3d^5$ having L = 0, S = 5/2), the crystalline anisotropy is small compared with Fe^{II} (with $[Ar]3d^6$ and L = 2, S = 2). Then depending on orientation, the external field would add vectorially to the local hyperfine field (which for Fe^{III} is antiparallel to the local moment). If, as we shall see below, moments do not realign in a large magnetic field, either the crystalline anisotropy is large (for example with Fe^{II}) or the magnetic interactions are *frustrated*. Frustration can be caused by competing exchange interactions that cannot all be satisfied, leading to complicated magnetic ground states (31). A Gaussian distribution was assumed for the remaining magnetic part as described by the average value $<B_{hf}>$ and standard deviation σ. We also simulated the spectra with an unconstrained histogram distribution, and the results were similar though the overall distributions were somewhat more variable from one spectrum to the next.

The indicated effective hyperfine field (Fig. 3, right side) was the vector sum of the true local hyperfine field and the external field. The area of the $ISC_{W/N}$ contribution (green

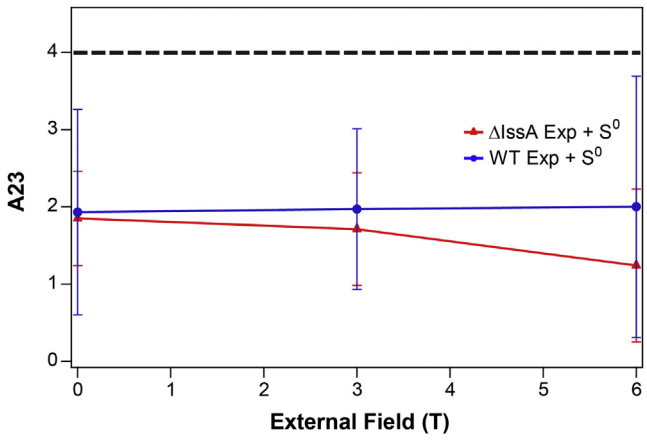

Figure 4. Plot of A_{23} *versus* external field for WT+S^0 and ΔIssA+S^0 exponential cells. *Blue line*, WT+S^0 cells; *Red line*, ΔIssA+S^0 cells. +S^0, growth that includes elemental sulfur.

line) was varied to minimize χ^2 error-residuals. The $ISC_{W/N}$ doublets represented 20% of the overall intensity. The calculated distributions of hyperfine fields for all three spectra were centered at $<B_{hf}>$ ~24 T with a Gaussian standard deviation of σ = 6 T. The distribution was essentially invariant up to a 6 T applied field. In addition, the relative intensities of lines 2 (and 5) with respect to lines 3 (and 4) did not change with applied fields, staying essentially equal to 2 up until at least 6 T (Fig. 4). This indicates that the magnetic system is remarkably rigid. In the case of Fe^{III}, this rigidity is unlikely to be due to crystalline anisotropy. A more likely explanation is that it arises from the frustration of the magnetic exchange interactions. Such processes are known for systems with antiferromagnetic interactions dominated by site-disorder or triangular lattices. In the current case, it seems more likely that the origin of the frustration is antiferromagnetic interactions and site disorder, similar to the properties of canonical spin glasses (31), or a disordered superparamagnetic material below the blocking temperature T_{BK}.

In contrast, the equivalent high-field low-temperature spectra of thioferrates exhibits a well-resolved six-line pattern (32). A similar six-line pattern is also observed for thioferrates in spectra collected at zero or low applied field. Thus, the magnetically ordered material in *P. furiosus*, obtained in WT+S^0 cells, does not have exactly the same magnetic properties as synthetic Na^+/K^+ thioferrates even though the high-temperature MB parameters are similar.

Superparamagnetic materials exhibit anti-Curie Law behavior and can be characterized by its T_{BK}. T_{BK} is operationally defined as the temperature at which half of the spectral intensity exhibits magnetic hyperfine interactions and half is collapsed into quadrupole doublets. To determine this for the TFL magnetic material in *P. furiosus*, we collected spectra at various temperatures (Fig. 5). Temperatures as high as ca. 135 K were required for all magnetic material to collapse into doublets; from this, we estimated $T_{BK} \approx 40$ to 50 K. In contrast, all magnetic material in spectra of synthetic thioferrates is collapsed between 4.2 K and 77 K (28), implying a slightly lower T_{BK}. This is another indication that the magnetic properties of the TFL material in *P. furiosus* differed in subtle ways from synthetic thioferrates.

To summarize these technical comments, the TFL material exhibits some magnetic properties that are similar to authentic thioferrates, but there are some physical/spectroscopic differences. We are unable to interpret these differences in an unambiguous manner to propose a chemically defined structure for this novel material, so we can only conclude that it is thioferrate-*like*.

After collecting these spectra, the sample was thawed, and the metal contents determined (Table S5). The iron concentration in the WT+S^0 sample was 5.25 mM—about 5-fold higher than the WT-S^0 sample. Most or all of this additional iron was due to the TFL iron described above. If the expression levels of the $[Fe_4S_4]$-containing proteins were unchanged with the added sulfur, ca. 20% of the spectral intensity should have

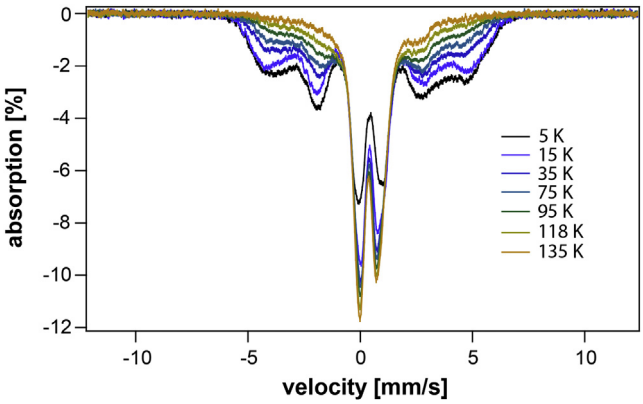

Figure 5. Low-field (0.05 T) Mössbauer spectra of exponentially harvested WT+S^0 cells collected at increasing temperatures. +S^0, growth that includes elemental sulfur.

been $ISC_{W/N}$ doublets. This is within our estimate of 10% to 20%. Our data (weakly) support a slight decline in the expression levels of the $[Fe_4S_4]$-containing proteins when S^0 is included in the medium. Also noteworthy is that WT+S^0 cells contained significantly higher concentrations of Cu, Mn, and Zn than WT-S^0 cells (Table S5), indicating a widespread S^0-dependent shift in metal-associated processes.

WT cells harvested in stationary state

We next collected MB spectra of WT cells grown as above, with and without S^0, but harvested at stationary state. Both 5 K and 150 K MB spectra of WT-S^0 cells (Fig. 6, *A* and *B*) were dominated by $ISC_{W/N}$ doublets that collectively accounted for ca. 75% of spectral intensity. Also evident were overlapping doublets due to at least two types of $Fe^{II}(O/N)_{5-6}$ species. Their collective intensity was ca. 23%, significantly greater than for samples harvested during exponential growth. No magnetic material was evident, and the only intense feature in the corresponding EPR spectrum was an isotropic signal at g = 2.00.

A minor $Fe^{II}(S)_4$ species was evident in the 150 K spectrum (Fig. 6*B*), as indicated by the arrow which highlights the low-energy line of the corresponding doublet. The solid green line simulates this species using parameters in Table 1. The doublet represented only ~2% of spectral intensity, but we observed it in multiple spectra. Such doublets are typical of Fe^{II} ions coordinated by a tetrahedral environment of sulfur donors. *P. furiosus* contains two proteins with such $Fe^{II}(S)_4$ sites, rubredoxin and rubrerythrin (Table S3).

The 5 K spectrum of WT+S^0 stationary state cells (Fig. 6*C*) was similar to that of exponentially growing WT+S^0 cells in that it was dominated by a broad feature spanning from −6 mm/s to +7 mm/s. This feature was assigned to the TFL material. Two intense lines near the center of the spectrum had parameters of $ISC_{W/N}$ doublets; they collectively represented no more than ~25% of spectral intensity as some portion of this was due to TFL material (Fig. 6*C*).

The magnetic hyperfine interactions associated with the TFL material were abolished at 150 K (Fig. 6*D*), with the

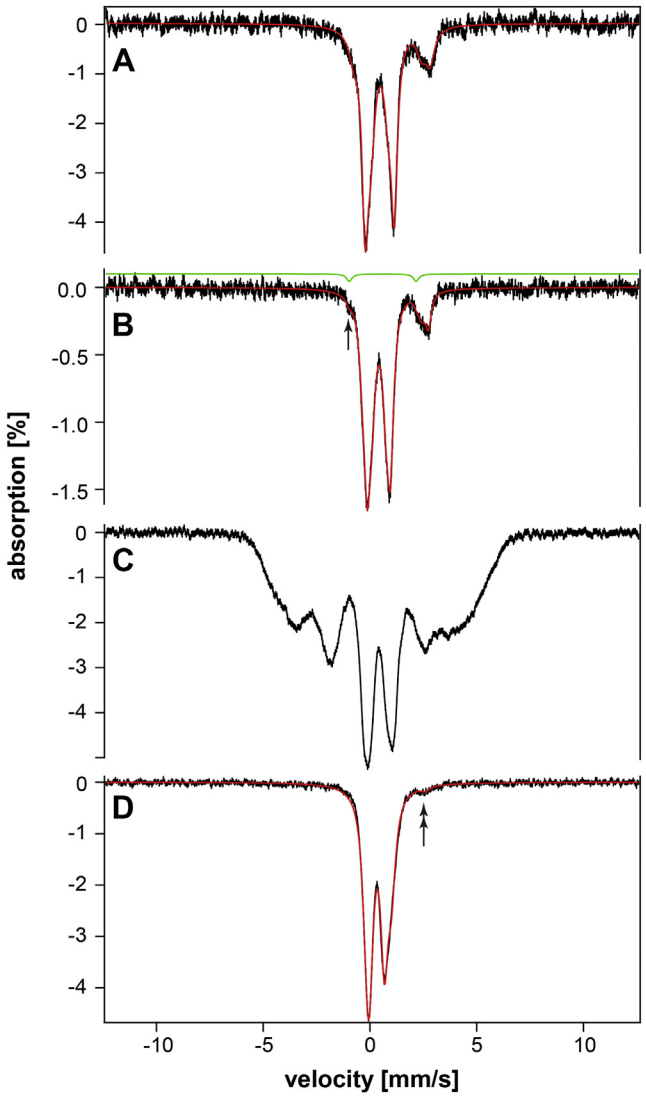

Figure 6. Low-field (0.05 T) Mössbauer spectra of WT cells harvested after reaching stationary state. *A*, WT-S^0, 5 K; *B*, WT-S^0, 150 K; *C*, WT+S^0, 5 K; *D*, WT+S^0, 150 K. -S^0, growth that excludes elemental sulfur; +S^0, growth that includes elemental sulfur.

intensity from this material collapsing over the $ISC_{W/N}$ doublets. As was observed with high-temperature spectra of exponentially grown cells, the ISC_N doublet became relatively more intense than the ISC_W doublet indicating that the TFL magnetic material collapsed mainly over the ISC_N doublet. A broad $Fe^{II}(O/N)_{5-6}$ doublet was also evident in the 150 K spectrum (arrow in Fig. 6*D*). Its intensity (~4%) was similar for the WT+S^0 sample harvested under exponential conditions but less than for the WT-S^0 sample harvested in stationary state.

After these spectra were collected, samples were thawed and analyzed for metal content. The iron concentrations in WT-S^0 and WT+S^0 cells were 660 μM and 8700 μM, respectively (Table S5). If the average expression level of $[Fe_4S_4]$-containing proteins remained unchanged with the addition of elemental sulfur, ~7% of the spectral intensity of Figure 6, *C* and *D* would be due to $ISC_{W/N}$. Our fitting analysis suggests slightly higher percentage range, namely 10% to 25%.

ΔIssA cells

The gene encoding the IssA protein is highly expressed under +S^0 conditions, and IssA is thought to be intimately involved in forming TFL nanoparticles. To investigate this further, we grew cells that lacked the gene encoding this protein, the ΔIssA strain, to determine whether it could form TFL iron. We first grew the deletion strain on the same medium as for WT-S^0 cells and harvested cells during exponential growth as a control. Their 10 K 0.05 T MB spectrum (Fig. 7*A*) was dominated by the $ISC_{W/N}$ doublets (~80% total). The spectrum also exhibited a broad doublet because of at least two $Fe^{II}(O/N)_{5-6}$ species, representing 12% of the overall intensity (double arrows on the right), and to a minor $Fe^{II}(S)_4$ doublet representing ~3% of the intensity (single arrows). The 150 K spectrum (Fig. 7*B*) exhibited the same features, with the temperature-dependence of the $ISC_{W/N}$ doublets visually apparent and both Fe^{II} doublets better resolved. The 4.2 K 6.0 T spectrum (Fig. 7*C*) was simulated assuming that the $ISC_{W/N}$ doublets were diamagnetic, confirming that they arose from S = 0 $[Fe_4S_4]^{2+}$ clusters.

ΔIssA+S^0 cells were grown and harvested similarly. Their low-temperature MB spectra exhibited an intense six-line spectra at all applied fields (Fig. 8, *A*–*C*). Most or all of the spectral intensity arose from the TFL material. The peaks were better resolved than the corresponding spectral features in the WT+S^0 spectra, implying some IssA-dependent structural

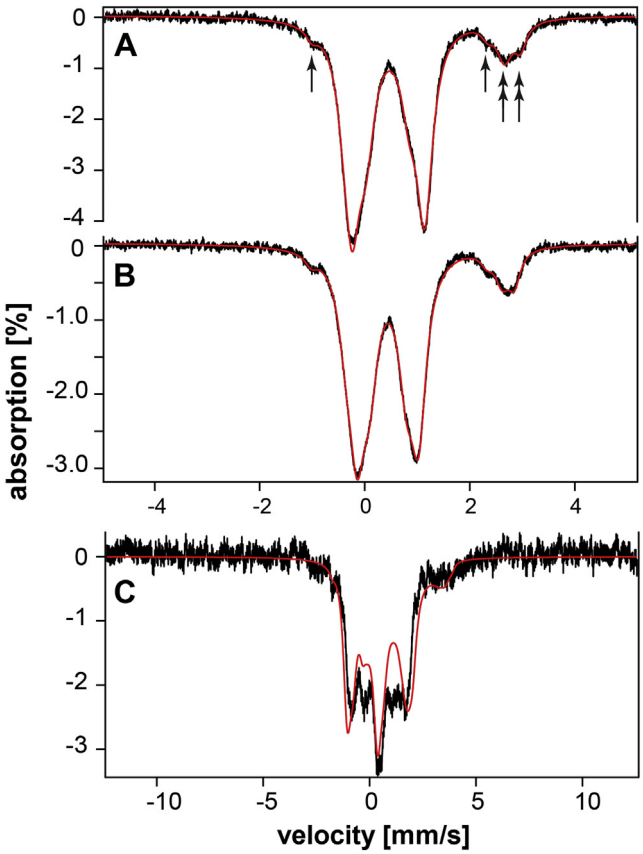

Figure 7. Mössbauer spectra of ΔIssA-S^0 cells. *A*, 10 K and 0.05 T; *B*, 150 K and 0.05 T; *C*, 4.2 K and 6.0 T. -S^0, growth that excludes elemental sulfur.

differences. Surprisingly, the positions of the lines were *unaffected* by applied fields as high as 6.0 T, though the linewidths broadened with increasing field. This implied that the magnetic coupling between particles in the material was significantly stronger than the applied fields and could not be broken at 6 T.

Technical details regarding the physical properties of the TFL material in ΔIssA+S⁰ cells

Again, the following are technical details that can be skipped without loss of continuity. There were several differences in the magnetism of the ΔIssA+S^0 sample compared with the WT+S^0 exponential sample. Specifically, the extent of broadening of the distribution with external field was greater, and there was a gradual change in the relative line intensity A_{23} (Fig. 4).

Antiferromagnets orient perpendicular to an external field when the crystalline anisotropy is not excessive. In that case, all moments would be in a plane that includes the gamma rays. Kuncser *et al.* (29, 30) has given several expressions for A_{23} in different cases. Using their result for moments in a plane with the gamma ray (see Ref (30), Eq. 7'), we obtain A_{23} = 4/3 = 1.33, which is about what is observed for an external field of 6 T. Thus, the interactions appear to be strongly antiferromagnetic but with less crystalline anisotropy or frustration than in the WT+S^0 exponential sample.

We also collected low-field spectra at increasing temperatures (Fig. 9) to observe the loss of magnetic hyperfine interactions. Both Gaussian and Histogram models were fitted to the spectra. Average results for the two methods (average B_{hf}, width of the distribution $P(B_{hf})$) were similar. Fits assuming the Gaussian model broadened dramatically at 55 K, caused by a strong increase of a low field component. T_{BK} was ~50 K, similar to that obtained for the TFL nanoparticles in WT+S^0 cells. Determining the magnetic component for temperatures above 55 K was difficult because of overlap with the $ISC_{W/N}$ components. However, the transition with increasing temperatures was similar to the superparamagnetism observed in fine grains (33). The linewidths for $ISC_{W/N}$ components remained remarkably sharp with increasing temperatures (Table 1).

In summary, these technical details describe how the TFL nanoparticles in ΔIssA+S^0 cells are somewhat different from those in WT+S^0 cells. Again, we are unable to interpret those differences in unambiguous chemical/structural terms apart from concluding that the material is more crystalline/homogenous in the absence of IssA.

After spectra were collected, the sample were thawed, and cellular metal and overall protein concentrations were determined; the protein concentrations in ΔIssA-S^0 and ΔIssA-S^0 samples were 78 ± 3 mg/ml and 36 ± 2 mg/ml, respectively. Metal concentrations are in Table S5.

Growth experiments

Two roles have been proposed for IssA; that it is involved in Fe storage or that it serves to detoxify insoluble FeS clusters (22, 23). To test the role of IssA in Fe storage, WT cells were harvested after growth under +S^0 and -S^0

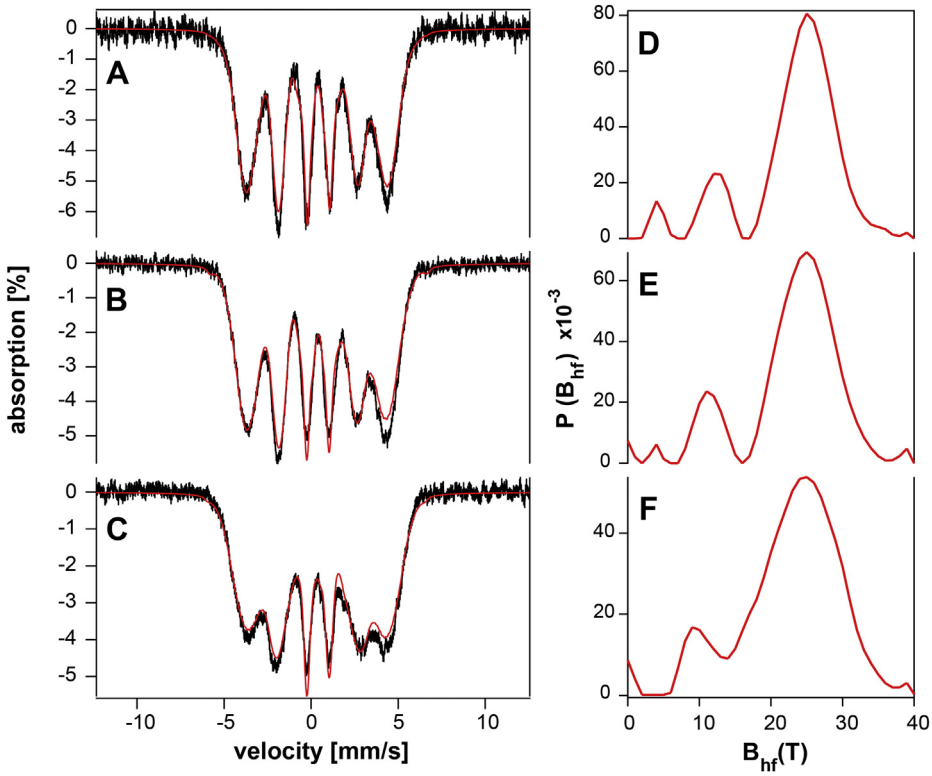

Figure 8. 4.2 K Mössbauer spectra of ΔIssA+S^0 cells at different applied fields. *A*, 0; *B*, 3.0; *C*, 6.0 T. Unconstrained histogram distributions are shown in *D* (0 T), *E* (3 T), and *F* (6 T). +S^0, growth that includes elemental sulfur.

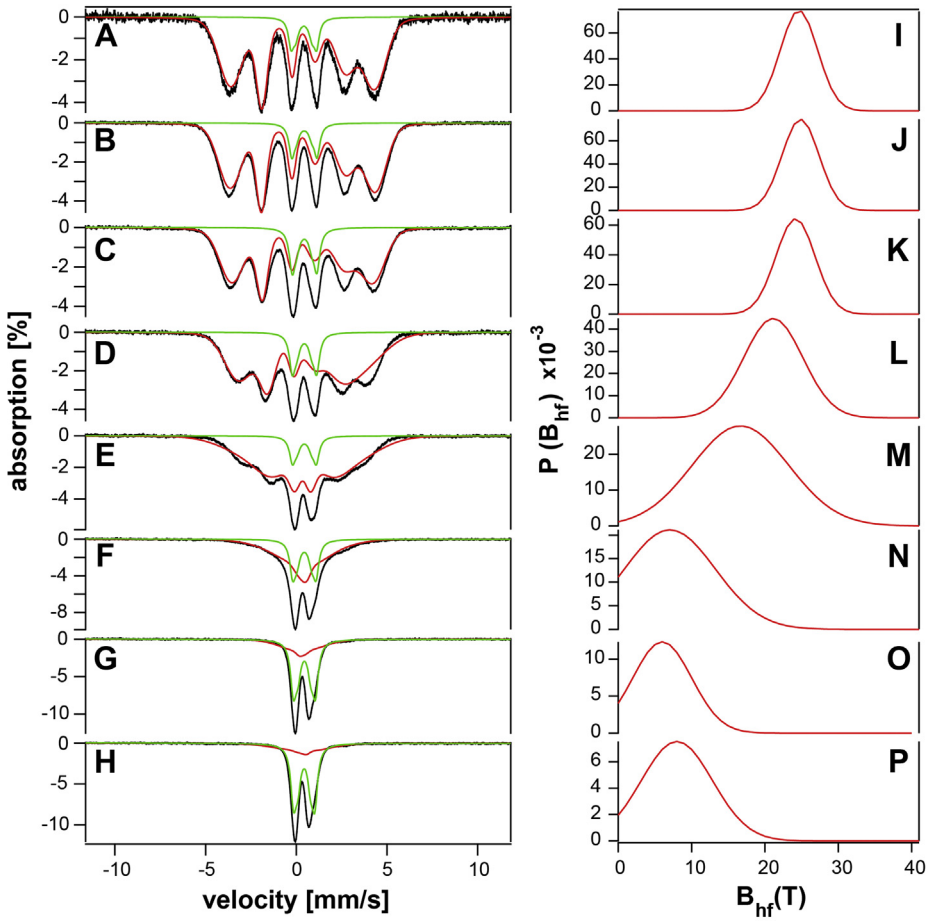

Figure 9. Variable temperature 0.05 T Mössbauer spectra of ΔIssA +S^0 cells. *Right column* shows the B_{hf} distribution used to obtain the fit. *A* and *I*, 5 K; *B* and *J*, 10 K; *C* and *K*, 25 K; *D* and *L*, 40 K; *E* and *M*, 55 K; *F* and *N*, 70 K; *G* and *O*, 100 K; *H* and *P*, 120 K. Solid *green lines* in the *left column* show contribution from $ISC_{N/W}$ while *solid red lines* indicate contribution from TFL. +S^0, growth that includes elemental sulfur; TFL, thioferrate-like.

conditions, and ΔIssA under +S^0 conditions. The harvested cells were washed and used to inoculate iron-depleted medium; if IssA binding of TFL aggregates serves to increase the bioavailability of the iron, only WT+S^0 cells should have grown in this iron-depleted medium. However, there was no growth in any of the iron-depleted medium, no matter what cells were used to inoculate the medium (data not shown).

To test whether IssA is used to detoxify insoluble Fe/S aggregates, WT and ΔIssA strains were grown with and without adding 50 μM iron in both 10 mM sodium sulfide medium (low IssA expression, Fig. 10*A*) and 1 g/l S^0 medium (High IssA expression, Fig. 10*B*). Under low sulfide concentrations, all strains grew to similarly high cell protein concentrations in culture (∼90 μg/ml), suggesting that high iron concentrations by themselves are not toxic to the cell. On the other hand, under + S^0 (high sulfide) conditions, increasing the Fe concentration led to a significant decrease in growth in both WT and ΔIssA strains. Additionally, the ΔIssA strain only reached half the cell protein concentration as WT under normal (10 μM) Fe conditions, suggesting that IssA sequesters iron, in the presence of sulfur, that would otherwise be toxic.

Discussion

Our results demonstrate that the iron content or ironome of *P. furiosus* cells changes dramatically when elemental sulfur is added to the growth medium. Under -S^0 conditions, most of the iron in the cell is S = 0 $[Fe_4S_4]^{2+}$ clusters. Under +S^0 conditions, the cell imports ∼5 times more iron, with 75 to 90% eventually forming TFL aggregates. Some of the iron in WT+S^0 cells must have been in the form of $[Fe_4S_4]^{2+}$ clusters, but quantifying how much was in this form proved difficult because the MB spectral features of TFL iron were indistinguishable from those of $[Fe_4S_4]^{2+}$ clusters at high temperatures, and at low temperatures, the contribution of diamagnetic $[Fe_4S_4]^{2+}$ clusters was obscured by the dominating magnetic features of the TFL aggregates. Simulations of the low-temperature spectral pattern of the ΔIssA+S^0 cells indicated that the $[Fe_4S_4]$ contribution was negligible. All things considered, we tentatively conclude that the overall expression level of $[Fe_4S_4]$-containing proteins *decreases* somewhat under +S^0 conditions. This supports a shift in cellular metabolism when elemental sulfur is present. $[Fe_4S_4]$-containing hydrogenases are downregulated under +S^0 conditions (13), and cells grow faster under +S^0 conditions as long as sufficient iron is included in the growth media. We also found that

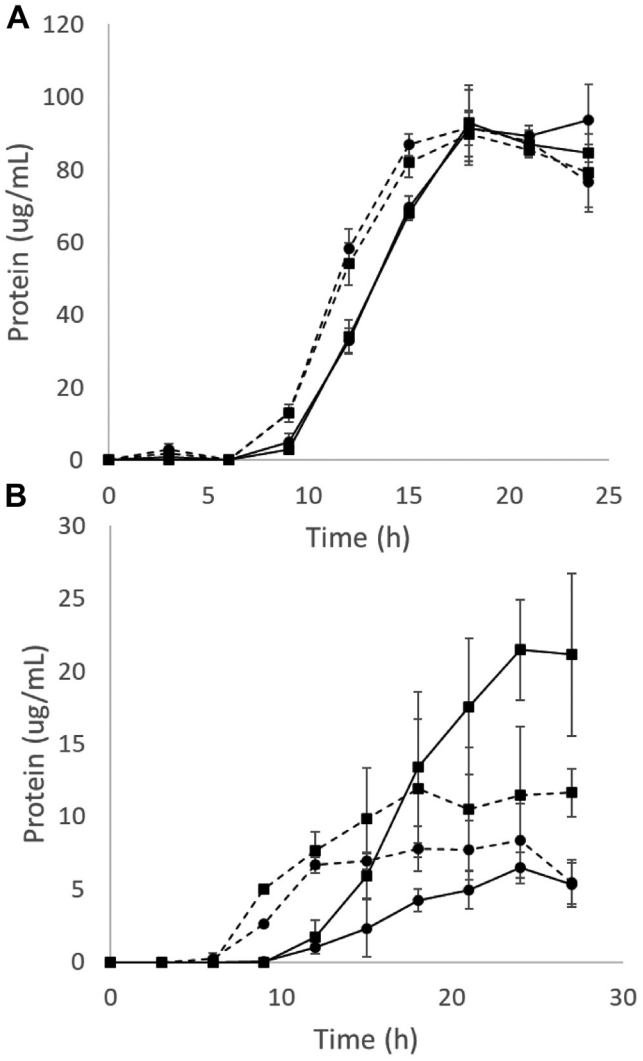

Figure 10. Growth of *Pyrococcus furiosus* on maltose and under different sulfur conditions. *Top panel*, with 10 mM Na_2S; *Bottom panel*, with 1 g/l S^0. *Solid lines*, WT; *dashed lines*, ΔIssA; (■), 10 μM Fe; (●), 50 μM Fe. Error bars represent standard deviation of biological triplicate samples.

concentrations of other metals (Cu, Mn, Zn) were significantly higher in cells grown under $+S^0$ conditions, again indicating major metal-associated metabolic changes.

We characterized the TFL iron in $+S^0$ cells. This material is closely related to authentic thioferrates in that both consist predominantly of Fe^{III} ions coordinated to four sulfide ions in a tetrahedral geometry. Neither form of iron contains *localized* $Fe^{II}(S)_4$ units, but we cannot exclude the possibility that TFL iron includes some *delocalized* [Fe^{II} Fe^{III}] units. This situation is found in [Fe_4S_4] clusters which have virtually the same δ and ΔE_Q values as TFL iron.

At low temperatures, authentic sodium thioferrate ($NaFeS_2$) exhibits a well-resolved sextet including magnetic hyperfine interactions of magnitude 270 kG (28). This hyperfine field is unusually small for ferric ions because of a high degree of covalency with sulfur. Using MB spectroscopy, Zink and Kargony (32) examined authentic $KFeS_2$ at variable applied perpendicular fields up to 5 T. At all applied fields, synthetic thioferrates displayed a sextet that was not strongly affected by the field. Similarly, the TFL material in both WT+S^0 and ΔIssA+S^0 cells was not strongly affected by applied fields up to 6 T. This suggests even stronger interactions in TFL iron than in synthetic thioferrates. The spectra again show line-splittings characteristic of magnetic ordering including line broadening typical of a continuous distribution of hyperfine fields. ΔIssA+S^0 spectra were analyzed assuming no ISC contribution.

One of the most surprising conclusions from this work is that the IssA protein is not required for forming TFL particles as these particles formed in *P. furiosus* cells lacking IssA. In fact, the spectral properties of TFL particles in the absence of this protein were closer to synthetic thioferrates as they exhibited a well-resolved six-line pattern at 5 K. The poorer spectral resolution associated with the TFL material in WT+S^0 cells may be due to a more heterogeneous distribution of TFL structures. We considered that IssA disrupts the thioferrate structure, perhaps making the material more bioavailable to the cell, but it does not appear to do so.

We also examined the temperature-dependence of hyperfine interactions and used both Gaussian and Histogram models to fit the spectra. Average results for the two methods (average $<B_{hf}>$, width of the distribution P(Bhf)) were similar. Fits assuming the Gaussian model broadened dramatically at 55 K, caused by a strong increase of a low-field component. Determining this component for temperatures above 55 K was made difficult by the overlap with the $ISC_{W/N}$ components. However, the transition with increasing temperatures was similar to the superparamagnetism of fine grains (33).

By 77 K, these interactions are fully abolished in synthetic thioferrates, whereas some interactions remained at this temperature in the *P. furiosus* TFL aggregates. T_{BK} of the TFL material is thus slightly higher than for authentic thioferrates. T_{BK} reflects the size of the magnetically interacting particles, suggesting somewhat larger particles for TFL material in $+S^0$ *P. furiosus* cells.

Exponentially growing *P. furiosus* -S^0 cells contained only 2 to 5% high-spin $Fe^{II}(O/N)_{5-6}$ sites. In contrast, *E. coli* and *B. subtilis* (Gram negative and positive bacteria) contain substantially higher concentrations of such species (24). The percentage of $Fe^{II}(O/N)_{5-6}$ in *P. furiosus* -S^0 cells increased as they shifted from exponential to stationary state. We hypothesize that imported Fe^{II} is used to assemble and install ISCs into proteins and to metallate proteins with mononuclear Fe and Fe-O-Fe active sites. Perhaps, the rates of these assembly and metallation activities decline in stationary state, causing the Fe^{II} feedstock to accumulate. Under $+S^0$ conditions, the demand for imported Fe^{II} may be greater (for use in generating large amounts of TFL iron), causing the level of Fe^{II} in such cells to remain low under stationary state conditions.

P. furiosus -S^0 cells also contain a small percentage contribution of $Fe^{II}(S)_4$ sites, corresponding to roughly 10 to 40 μM cellular iron. A similar concentration might be present in $+S^0$ cells, but such sites could not be detected (likely because of the higher concentration of cellular iron). Table S2 indicated just two proteins that contain such sites, namely rubredoxin and

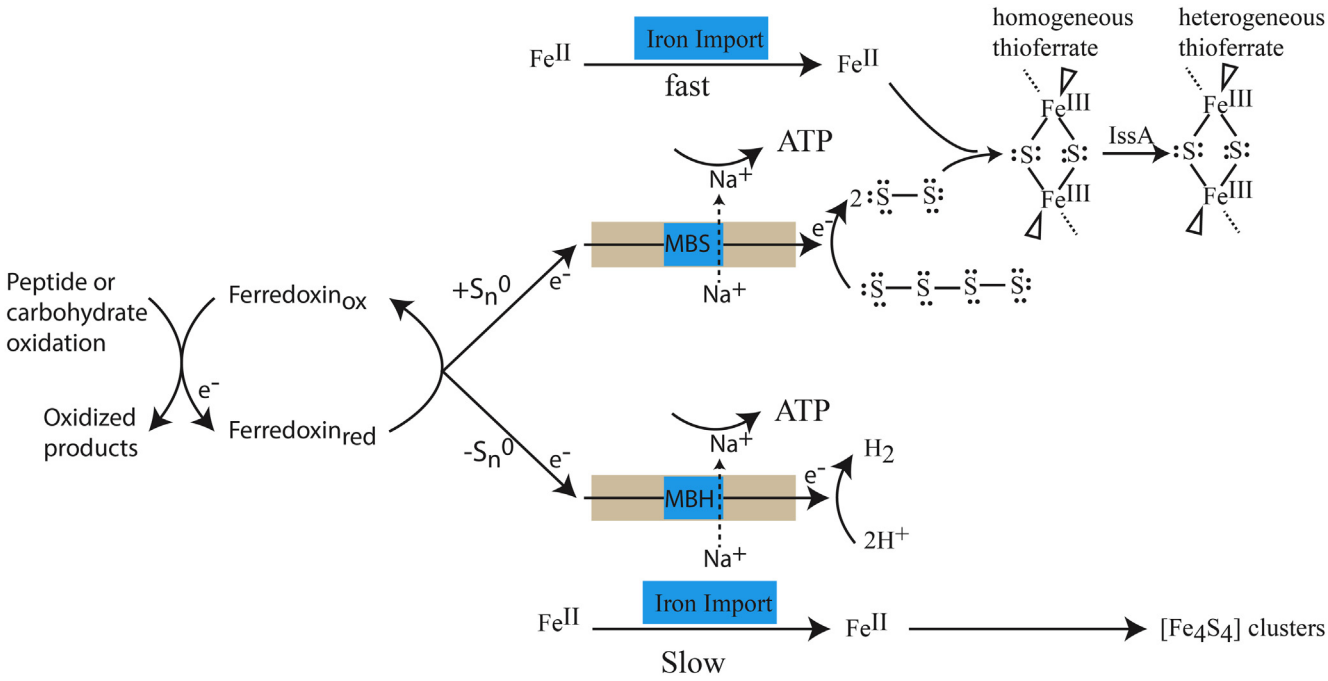

Figure 11. A Model of cellular energy metabolism emphasizing the role of iron and elemental sulfur in *P. furiosus*. See text for details. MBH, membrane-bound respiratory hydrogenase; MBS, membrane-bound sulfane reductase.

rubrerythrin. This suggests an average cellular concentration of roughly 10 μM each for these proteins.

The TFL material was thought to store iron, coordinated by IssA protein in large assemblies reminiscent of how Fe^{III} is stored in ferritins (23), but other possibilities should now be considered. It seems unlikely that $+S^0$ cells would store huge amounts of iron, whereas $-S^0$ cells would store none, even when both are grown under the same iron-replete conditions. Our experiments have shown that cells in which iron is stored as IssA-bound thioferrate cannot use it as an iron source when transferred to iron-depleted medium. In contrast, *E. coli* cells accumulate large amounts of iron as Fe^{II} (perhaps for storage), yeast accumulates Fe^{III} polyphosphate in vacuoles (34), and human cells store Fe^{III} as nanoparticles in ferritin cores (26). As a strict anaerobe, *P. furiosus* may not need to store much iron because Fe^{II} dominates the environment under anaerobic conditions and is far more soluble (and thus more bioavailable) than Fe^{III} under the more common aerobic conditions.

Clarkson *et al.* (22) suggested that IssA is used to sequester insoluble iron sulfides that may be toxic to the cell, as IssA expression is sulfide specific and dependent on the presence of iron. The growth experiments conducted in this study support this hypothesis, as high Fe concentrations had no effect on growth of either the parent or ΔIssA in the absence of sulfide, and whereas iron was still predominantly stored as TFL material in the absence of IssA, the ΔIssA strain showed a significant negative growth phenotype compared with the parent under high sulfide and high Fe conditions.

In light of this, we tentatively propose a new role of TFL iron in the metabolism of *P. furiosus* (Fig. 11). Cells grown under $-S^0$ conditions use membrane-bound hydrogenase as a redox-dependent proton pump to generate a Na^+ ion gradient that is subsequently used to generate ATP *via* chemiosmosis. Here, H^+ ions are used as the terminal electron acceptor in the electron transport chain, using reducing equivalents that originate from the oxidation of either peptides or carbohydrates and are then channeled through ferredoxin. Imported Fe^{II} is used to generate $[Fe_4S_4]$ clusters, among other processes, and these are installed into various apo-proteins including hydrogenases.

Under $+S^0$ conditions, the expression level of membrane-bound MBH decreases, the expression level of membrane-bound MBS increases (Table S3), and the rate of Fe^{II} import increases. Using reducing equivalents also obtained from peptides or carbohydrates (and also trafficked through the ferredoxin), sulfane sulfur reductase catalyzes the reduction of imported polysulfides. Thus, polysulfides serve as the terminal electron acceptor in this form of anaerobic respiration, replacing protons under $+S^0$ conditions. We speculate that free short polysulfide chains are toxic to the cell and that they react with Fe^{II} to generate the TFL material which, when bound to IssA, is less toxic to the cell. In essence, TFL iron might be a waste product of S^0-dependent anaerobic respiration. As the cell grows, its volume increases along with an increasing concentration of the TFL iron such that the net balance of the opposing processes results in 5 to 9 mM cellular iron concentration. The rate of $[Fe_4S_4]$ synthesis may decline under $+S^0$ conditions because demand is reduced. It is intriguing to consider that this may have been an ancient respiratory pathway that dominated the early Earth in locations where elemental sulfur and ferrous ions were abundant but O_2 pressures were low.

Experimental procedures

Cell growth

Strains used in this study are listed in Table S6. Cultures for MB experiments were grown in defined maltose media composed of 1× base salts, 1× trace minerals, 1× vitamin solution, 2× 19-amino-acid solution, 0.5% (wt/vol) maltose, 0.1% (wt/vol) yeast extract, 10 μM sodium tungstate, and 0.25 mg/ml resazurin, with added cysteine at 0.5 g/l, sodium bicarbonate at 1 g/l, and 1 mM sodium phosphate buffer (pH 6.8). The 5× base salts stock solution contained (per liter) 140 g of NaCl, 17.5 g of $MgSO_4{\cdot}7H_2O$, 13.5 g of $MgCl_2{\cdot}6H_2O$, 1.65 g of KCl, 1.25 g of NH_4Cl, and 0.70 g of $CaCl_2{\cdot}2H_2O$. The 1000× trace mineral stock solution contained (per liter) 1 ml of HCl (concentrated), 0.5 g of Na_4EDTA, 0.05 g of H_3BO_3, 0.05 g of $ZnCl_2$, 0.03 g of $CuCl_2{\cdot}2H_2O$, 0.05 g of $MnCl_2{\cdot}4H_2O$ 0.05 g of $(NH_4)_2MoO_4$, 0.05 g of $AlK(SO_4){\cdot}2H_2O$, 0.05 g of $CoCl_2{\cdot}6H_2O$, and 0.05 g of $NiCl_2{\cdot}6H_2O$. The 200× vitamin stock solution contained (per liter) 10 mg each of niacin, pantothenate, lipoic acid, *p*-aminobenzoic acid, thiamine (B_1), riboflavin (B_2), pyridoxine (B_6), and cobalamin (B_{12}) and 4 mg each of biotin and folic acid. The 25× 19-amino-acid solution contained (per liter) 3.125 g each of arginine and proline; 1.25 g each of aspartic acid, glutamine, and valine; 5.0 g each of glutamic acid and glycine; 2.5 g each of asparagine, histidine, isoleucine, leucine, lysine, and threonine; 1.875 g each of alanine, methionine, phenylalanine, serine, and tryptophan; and 0.3 g tyrosine. ^{57}Fe was added from a 50 μM stock solution prepared by dissolving 6 mg of elemental ^{57}Fe in 200 μl of a 1:3 HNO_3:HCl mixture. The $+S^0$ conditions contained added S^0 at 3 g/l.

Five hundred milliliter cultures were grown anaerobically in 1 l culture bottles at 90 °C with shaking. Cells were harvested at the desired timepoints by centrifugation at 18,000*g* for 10 min in a Beckman-Coutler Avanti J-30i centrifuge. The cell pellets were washed 3× with 2× base salts containing 50 μM sodium dithionite. Cells were loaded into MB cups and frozen at −80 °C.

For additional growth experiments, the medium was prepared as described above but with the following substitutions: yeast extract and ^{57}Fe were omitted from the medium, $FeCl_3$ was added from a 10 mM stock solution, and 50 mM 3-(N-morpholino)propanesulfonic acid was added. For FeS toxicity experiments, sulfide (as Na_2S) or S^0 were added as indicated. Strains were grown in 50 ml culture bottles at 90 ℃ with shaking. For iron bioavailability experiments, cultures were first grown in medium containing 10 μM iron with (WT and ΔIssA) and without (WT only) 3 g/l added S^0. Cultures were harvested by centrifugation at 18,000*g* for 10 min in a Beckman Coulter Microfuge 22 Centrifuge. Cell pellets were washed 3× in 20 mM imidazole pH 6.5 containing 30 mM $MgCl_2{\cdot}6H_2O$, 0.5 M KCl, 2 mM cysteine-HCl, 2 mM dithionite, and 2 mM dithiothreitol and resuspended in the same buffer. Cell suspensions were used to inoculate defined medium containing an additional 30 μM bathophenanthroline disulfonic acid. For both growth experiments, 1 ml culture samples were taken at desired time intervals, and cell protein was measured using a standard Bradford protein assay.

Mössbauer and EPR spectroscopies

Low-field MB spectra were collected using a model MS4 spectrometer (SEE Co). High-field spectra were collected at 4.2 K using a model L: He-6T spectrometer. Spectra were analyzed using WMOSS software. In spectra that contains both TFL iron and ISC doublets, the doublets were simulated using a spin Hamiltonian model (SpinHam option in WMOSS) using parameters obtained from spectra that did not contain TFL iron. Then, the area of the doublets was allowed to vary in the WinNormos program keeping all other parameters (including hyperfine) constant. Isomer shifts are reported relative to α-Fe foil at room temperature. Following MB analysis, samples were thawed in an anaerobic glovebox, transferred into EPR tubes, and refrozen. Continuous-wave X-band EPR spectra were collected using a Bruker Elexsys E500A spectrometer with a cryogen-free cooling system.

Metal and protein analyses

After spectra were collected, samples were thawed and transferred quantitatively to preweighed 15 ml Falcon tubes, and weighed again. The difference, after subtracting the buffer contribution, was taken as the mass of the cells. Samples were resuspended in 5 mg deionized H_2O per gram of cells. Two mg of 0.5 mm diameter glass beads (Sigma) were added per mg of resuspended cell pellet, and the mixture was vortexed 3× for 30 s followed by 1 min on ice. The resulting lysate was centrifuged at 14,000*g*, and the protein concentration of the supernatant was determined using the Pierce BCA Protein Assay Kit (Thermo Scientific). To the same, supernatant was added an equal volume of trace-metal grade nitric acid, and the solution was sealed and heated overnight at 80 °C. Samples were diluted with distilled deionized water and analyzed by ICP-MS (Agilent 7700x).

Data availability

All data are contained within the manuscript and SI.

Supporting information—This article contains supporting information (3, 6, 11, 14, 19–23, 35–60).

Acknowledgments—We thank Dr Francis Jenney for the gift of ^{57}Fe.

Author contributions—S. W. V. collected and analyzed the Mössbauer spectra, prepared most figures, and helped write the article. D. K. H. grew cells, performed the experiments involving cell growth, and prepared some figures. R. A. B. analyzed the magnetic properties of the TFL material. M. W. W. A. conceived of the project and analyzed the cell biological implications. P. A. L. designed the project, analyzed the results, and wrote the first draft of the article. All authors modified/edited the article and approved of its publication.

Funding and additional information—This work was supported by the National Institutes of Health (GM127021 to P. A. L.), the National Science Foundation (MCB-1817389), the Robert A. Welch Foundation (A1170), and the Division of Chemical Sciences, Geosciences and Biosciences, Office of Basic Energy Sciences of the Department of Energy (DE-FG02-95ER20175 to M. W. W. A.). The content is solely the responsibility of the authors and does not necessarily represent the official views of the National Institutes of Health, the National Science Foundation, the Welch Foundation or the Department of Energy.

Conflict of interest—The authors declare that they have no conflicts of interest with the contents of this article.

Abbreviations—The abbreviations used are: AOR, aldehyde ferredoxin oxidoreductase; EPR, electron paramagnetic resonance; ISC, iron sulfur cluster; MB, Mössbauer; MBH, membrane-bound respiratory hydrogenase; MBS, membrane-bound sulfane reductase; $+S^0$, growth that includes elemental sulfur; $-S^0$, growth that excludes elemental sulfur; T_{BK}, blocking temperature; TFL, thioferrate-like.

References

1. Fiala, G., and Stetter, K. O. (1986) *Pyrococcus furiosus* sp. nov represents a novel genus of marine heterotrophic archaebacteria growing optimally at 100°C. *Arch. Microbiol.* **145**, 56–61
2. Cvetkovic, A., Menon, A. L., Thorgersen, M. P., Scott, J. W., Poole, F. L., Jenney, F. E., Lancaster, W. A., Praissman, J. L., Shanmukh, S., Vaccaro, B. J., Trauger, S. A., Kalisiak, E., Apon, J. V., Siuzdak, G., Yannone, S. M., *et al.* (2010) Microbial metalloproteomes are largely uncharacterized. *Nature* **466**, 779–782
3. Lancaster, W. A., Praissman, J. L., Poole, F. L., Cvetkovic, A., Menon, A. L., Scott, J. W., Jenney, F. E., Jr., Thorgersen, M. P., Kalisiak, E., Apon, J. V., Trauger, S. A., Siuzdak, G., Tainer, J. A., and Adams, M. W. W. (2011) A computational framework for proteome-wide pursuit and prediction of metalloproteins using ICP-MS and MS/MS data. *BMC Bioinformatics* **12**, 64
4. Andreini, C., Banci, L., Bertini, I., Elmi, S., and Rosato, A. (2007) Non-heme iron through the three domains of life. *Proteins* **67**, 317–324
5. Robb, F. T., Maeder, D. L., Brown, J. R., DiRuggiero, J., Stump, M. D., Yeh, R. K., Weiss, R. B., and Dunn, D. M. (2001) Genomic sequence of hyperthermophile, Pyrococcus furiosus: Implications for physiology and enzymology. *Methods Enzymol.* **330**, 134–157
6. Mukund, S., and Adams, M. W. W. (1991) The novel tungsten-iron-sulfur protein of the hyperthermophilic archaebacterium, *Pyrococcus furiosus*, is an aldehyde ferredoxin oxidoreductase. Evidence for its participation in a unique glycolytic pathway. *J. Biol. Chem.* **266**, 14208–14216
7. Mukund, S., and Adams, M. W. W. (1990) Characterization of a tungsten-iron-sulfur protein exhibiting novel spectroscopic and redox properties from the hyperthermophilic archaebacterium *Pyrococcus furiosus*. *J. Biol. Chem.* **265**, 11508–11516
8. Ozawa, Y., Nakamura, T., Kamata, N., Yasujima, D., Urushiyama, A., Yamakura, F., Ohmori, D., and Imai, T. (2005) *Thermococcus profundus* 2-ketoisovalerate ferredoxin oxidoreductase, a key enzyme in the archaeal energy-producing amino acid metabolic pathway. *J. Biochem.* **137**, 101–107
9. Heider, J., Mai, X., and Adams, M. W. W. (1996) Characterization of 2-ketoisovalerate ferredoxin oxidoreductase, a new and reversible coenzyme A-dependent enzyme involved in peptide fermentation by hyperthermophilic archaea. *J. Bacteriol.* **178**, 780–787
10. Ma, K., Hutchins, A., Sung, S. J. S., and Adams, M. W. W. (1997) Pyruvate ferredoxin oxidoreductase from the hyperthermophilic archaeon, *Pyrococcus furiosus*, functions as a CoA-dependent pyruvate decarboxylase. *Proc. Natl. Acad. Sci. U. S. A.* **94**, 9608–9613
11. Yu, H. J., Wu, C.-H., Schut, G. J., Haja, D. K., Zhao, G. P., Peters, J. W., Adams, M. W. W., and Li, H. L. (2018) Structure of an ancient respiratory system. *Cell* **173**, 1636–1649
12. Adams, M. W. W., Holden, J. F., Menon, A. L., Schut, G. J., Grunden, A. M., Hou, C., Hutchins, A. M., Jenney, F. E., Kim, C., Ma, K. S., Pan, G. L., Roy, R., Sapra, R., Story, S. V., and Verhagen, M. F. J. M. (2001) Key role for sulfur in peptide metabolism and in regulation of three hydrogenases in the hyperthermophilic archaeon *Pyrococcus furiosus*. *J. Bacteriol.* **183**, 716–724
13. Schut, G. J., Bridger, S. L., and Adams, M. W. W. (2007) Insights into the metabolism of elemental sulfur by the hyperthermophilic archaeon *Pyrococcus furiosus*: Characterization of a coenzyme A-dependent NAD(P)H sulfur oxidoreductase. *J. Bacteriol.* **189**, 4431–4441
14. Schut, G. J., Brehm, S. D., Datta, S., and Adams, M. W. W. (2003) Whole-genome DNA microarray analysis of a hyperthermophile and an archaeon: *Pyrococcus furiosus* grown on carbohydrates or peptides. *J. Bacteriol.* **185**, 3935–3947
15. Wu, C.-H., Schut, G. J., Poole, F. L., Haja, D. K., and Adams, M. W. W. (2018) Characterization of membrane-bound sulfane reductase: A missing link in the evolution of modern day respiratory complexes. *J. Biol. Chem.* **293**, 16687–16696
16. Lipscomb, G. L., Keese, A. M., Cowart, D. M., Schut, G. J., Thomm, M., Adams, M. W. W., and Scott, R. A. (2009) SurR: A transcriptional activator and repressor controlling hydrogen and elemental sulphur metabolism in *Pyrococcus furiosus*. *Mol. Microbiol.* **71**, 332–349
17. Lipscomb, G. L., Schut, G. J., Scott, R. A., and Adams, M. W. W. (2017) SurR is a master regulator of the primary electron flow pathways in the order Thermococcales. *Mol. Microbiol.* **104**, 869–881
18. Jenney, F. E., and Adams, M. W. W. (2001) Rubredoxin from Pyrococcus furiosus in hyperthermophilic enzymes Pt. C. *Methods Enzymol.* **334**, 45–55
19. Weinberg, M. V., Jenney, F. E., Jr., Cui, X., and Adams, M. W. W. (2004) Rubrerythrin from the hyperthermophilic archaeon *Pyrococcus furiosus* is a rubredoxin-dependent, iron-containing peroxidase. *J. Bacteriol.* **186**, 7888–7895
20. Strand, K. R., Sun, C. J., Jenney, F. E., Schut, G. J., and Adams, M. W. W. (2010) Oxidative stress protection and the repair response to hydrogen peroxide in the hyperthermophilic archaeon *Pyrococcus furiosus* and in related species. *Arch. Microbiol.* **192**, 447–459
21. Ramsay, B., Wiedenheft, B., Allen, M., Gauss, G. H., Lawrence, C. M., Young, M., and Douglas, T. (2006) Dps-like protein from the hyperthermophilic archaeon *Pyrococcus furiosus*. *J. Inorg. Biochem.* **100**, 1061–1068
22. Clarkson, S. M., Newcomer, E. C., Young, E. G., and Adams, M. W. W. (2010) The elemental sulfur-responsive protein (SipA) from the hyperthermophilic archaeon *Pyrococcus furiosus* is regulated by sulfide in an iron-dependent manner. *J. Bacteriol.* **192**, 5841–5843
23. Vaccaro, B. J., Clarkson, S. M., Holden, J. F., Lee, D. W., Wu, C. H., Poole, F. L., Cotelesage, J. J. H., Hackett, M. J., Mohebbi, S., Sun, J. C., Li, H. L., Johnson, M. K., George, G. N., and Adams, M. W. W. (2017) Biological iron-sulfur storage in a thioferrate-protein nanoparticle. *Nat. Commun.* **8**, 16110
24. Wofford, J. D., Bolaji, N., Dziuba, N., Outten, F. A., and Lindahl, P. A. (2018) Evidence that a respiratory shield in *Escherichia coli* protects a low-molecular-mass Fe^{II} pool from O_2-dependent oxidation. *J. Biol. Chem.* **294**, 50–62
25. Holmes-Hampton, G. P., Jhurry, N. D., McCormick, S. P., and Lindahl, P. A. (2013) Iron content of *Saccharomyces cerevisiae* cells grown under iron-deficient and iron-overload conditions. *Biochemistry* **52**, 105–114
26. Jhurry, N. D., Chakrabarti, M., McCormick, S. P., Holmes-Hampton, G. P., and Lindahl, P. A. (2012) Biophysical investigation of the ironome of human Jurkat cells and mitochondria. *Biochemistry* **51**, 5276–5284
27. Gütlich, P., Bill, E., and Trautwein, A. X. (2011) *Mössbauer Spectroscopy and Transition Metal Chemistry: Fundamentals and Applications*, Springer Verlag, Berlin and Heidelberg, Germany
28. Taft, C. A. (1977) Mössbauer studies of $NaFeS_2$: Magnetic hyperfine fields and covalency in $MFeS_2$ compounds (M = Na, K, Rb, Cs). *J. Phys.* **38**, 1161–1162
29. Kuncser, V., Keune, W., Vopsaroiu, M., and Bissell, P. R. (2002) The "in-plane" angular spin distribution in layered systems as obtained by Fe-57 Mössbauer spectroscopy. *Nucl. Instrum. Meth. B* **196**, 135
30. Kuncser, V., Keune, W., Vopsaroiu, M., and Bissell, P. R. (2006) The 'in-plane' angular spin distribution in layered systems as obtained by Fe-57 Mössbauer spectroscopy (vol 196, pg 135, 2002) (Erratum) *Nucl. Instrum. Meth. B* **245**, 539–542

31. Ramirez, A. P. (1994) Strongly geometrically frustrated magnets. *Annu. Rev. Mater. Sci.* **124**, 453–480
32. Zink, J., and Kagorny, K. (1988) Mössbauer spectroscopic investigations of the magnetic properties of potassium thioferrate-III. *J. Phys. Chem. Sol.* **49**, 1429–1434
33. Mørup, S., Topsøe, H., and Lipka, J. (1976) Modified theory for Mössbauer spectra of superparamagnetic particles: Application to Fe_3O_4. *J. Phys. Colloq.* **37**, C6-287–C6-290
34. Cockrell, A. L., Holmes-Hampton, G. P., McCormick, S. P., Chakrabarti, M., and Lindahl, P. A. (2011) Mössbauer and EPR study of iron in vacuoles from fermenting *Saccharomyces cerevisiae*. *Biochemistry* **50**, 10275–10283
35. Aono, S., Bryant, F. O., and Adams, M. W. W. (1989) A novel and remarkably thermostable ferredoxin from the hyperthermophilic archaebacterium *Pyrococcus furiosus*. *J. Bacteriol.* **171**, 3433–3439
36. Heltzel, A., Smith, E. T., Zhou, Z. H., Blamey, J. M., and Adams, M. W. W. (1994) Cloning, expression, and molecular characterization of the gene encoding an extremely thermostable [4Fe-4S] ferredoxin from the hyperthermophilic archaeon *Pyrococcus furiosus*. *J. Bacteriol.* **176**, 4790–4793
37. Tatur, J., Hagen, W. R., and Matias, P. M. (2006) A highly thermostable ferritin from the hyperthermophilic archaeal anaerobe *Pyrococcus furiosus*. *Extremophiles* **10**, 139–148
38. Ebrahimi, K. H., Hagedoorn, P. L., and Hagen, W. R. (2010) Inhibition and stimulation of formation of the ferroxidase center and the iron core in *Pyrococcus furiosus* ferritin. *J. Biol. Inorg. Chem.* **15**, 1243–1253
39. Roy, R., Mukund, S., Schut, G. J., Dunn, D. M., Weiss, R., and Adams, M. W. W. (1999) Purification and molecular characterization of the tungsten-containing formaldehyde ferredoxin oxidoreductase from the hyperthermophilic archaeon *Pyrococcus furiosus*: The third of a putative five-member tungstoenzyme family. *J. Bacteriol.* **181**, 1171–1180
40. Hu, Y. L., Faham, S., Roy, R., Adams, M. W. W., and Rees, D. C. (1999) Formaldehyde ferredoxin oxidoreductase from *Pyrococcus furiosus*: The 1.85 Å resolution crystal structure and its mechanistic Implications. *J. Mol. Biol.* **286**, 899–914
41. Roy, R., and Adams, M. W. W. (2002) Characterization of a fourth tungsten-containing enzyme from the hyperthermophilic archaeon *Pyrococcus furiosus*. *J. Bacteriol.* **184**, 6952–6956
42. Mukund, S., and Adams, M. W. W. (1995) Glyceraldehyde-3-phosphate ferredoxin oxidoreductase, a novel tungsten-containing enzyme with a potential glycolytic role in the hyperthermophilic archaeon *Pyrococcus furiosus*. *J. Biol. Chem.* **270**, 8389–8392
43. Mai, X., and Adams, M. W. W. (1994) Indolepyruvate ferredoxin oxidoreductase from the hyperthermophilic archaeon *Pyrococcus furiosus*. A new enzyme involved in peptide fermentation. *J. Biol. Chem.* **269**, 16726–16732
44. Mai, X., and Adams, M. W. W. (1996) Characterization of a fourth type of 2-keto acid-oxidizing enzyme from a hyperthermophilic archaeon: 2-ketogluatarate ferredoxin oxidoreductase from *Thermoccoccus litoralis*. *J. Bacteriol.* **178**, 5890–5896
45. Kletzin, A., and Adams, M. W. W. (1996) Molecular and phylogenetic characterization of pyruvate and 2-ketoisovalerate ferredoxin oxidoreductases from *Pyrococcus furiosus* and pyruvate ferredoxin oxidoreductase from *Thermotoga maritima*. *J. Bacteriol.* **178**, 248–257
46. Sapra, R., Verhagen, M. F. J. M., and Adams, M. W. W. (2000) Purification and characterization of a membrane-bound hydrogenase from the hyperthermophilic archaeon *Pyrococcus furiosus*. *J. Bacteriol.* **182**, 3423–3428
47. Yu, H., Haja, D. K., Schut, G. J., Wu, C. H., Meng, X., Zhao, G., Li, H., and Adams, M. W. W. (2020) Structure of the respiratory MBS complex reveals iron-sulfur cluster catalyzed sulfane sulfur reduction in ancient life. *Nat. Commun.* **11**, 5953
48. Nguyen, D. M. N., Schut, G. J., Zadvornyy, O. A., Tokmina-Lukaszewska, M., Poudel, S., Lipscomb, G. L., Adams, L. A., Dinsmore, J. T., Nixon, W. J., Boyd, E. S., Bothner, B., Peters, J. W., and Adams, M. W. W. (2017) Two functionally distinct NADPC-dependent ferredoxin oxidoreductases maintain the primary redox balance of *Pyrococcus furiosus*. *J. Biol. Chem.* **292**, 14603–14616
49. Hagen, W. R., Silva, P. J., Amorim, M. A., Hagedoorn, P. A., Wassink, H., Haaker, H., and Robb, F. T. (2000) Novel structure and redox chemistry of the prosthetic groups of the iron-sulfur flavoprotein sulfide dehydrogenase from *Pyrococcus furiosus*; evidence for a [2Fe-2S] cluster with $Asp(Cys)_3$ ligands. *J. Biol. Inorg. Chem.* **5**, 527–534
50. Charon, M. H., Volbeda, A., Chabriere, E., Pieulle, L., and Fontecilla-Camps, J. C. (1999) Structure and electron transfer mechanism of pyruvate:ferredoxin oxidoreductase. *Curr. Opin. Struct. Biol.* **9**, 663–669
51. Blamey, J. M., and Adams, M. W. W. (1993) Purification and characterization of pyruvate ferredoxin oxidoreductase from the hyperthermophilic archaeon *Pyrococcus furiosus*. *Biochim. Biophys. Acta* **1161**, 19–27
52. Kurihara, K., Tanaka, I., Chatake, T., Adams, M. W., Jenney, F. E., Jr., Moiseeva, N., Bau, R., and Niimura, N. (2004) Neutron crystallographic study on rubredoxin from *Pyrococcus furiosus* by BIX-3, a single-crystal diffractometer for biomacromolecules. *Proc. Natl. Acad. Sci. U. S. A.* **101**, 11215–11220
53. Bryant, F. O., and Adams, M. W. W. (1989) Characterization of hydrogenase from the hyperthermophilic archaebacterium, *Pyrococcus furiosus*. *J. Biol. Chem.* **264**, 5070–5079
54. Ma, K., Weiss, R., and Adams, M. W. W. (2000) Characterization of hydrogenase II from the hyperthermophilic archaeon *Pyrococcus furiosus* and assessment of its role in sulfur reduction. *J. Bacteriol.* **182**, 1864–1871
55. Yeh, A. P., Hu, Y., Jenney, F. E., Adams, M. W. W., and Rees, D. C. (2000) Structures of the superoxide reductase from *Pyrococcus furiosus* in the oxidized and reduced states. *Biochemistry* **39**, 2499–2508
56. Clay, M. D., Jenney, F. E., Jr., Hagedoorn, P. L., George, G. N., Adams, M. W. W., and Johnson, M. K. (2002) Spectroscopic studies of *Pyrococcus furiosus* superoxide reductase: Implications for active-site structures and the catalytic mechanism. *J. Am. Chem. Soc.* **124**, 788–805
57. Jenney, F. E., Jr., Verhagen, M. F. J. M., Cui, X., and Adams, M. W. W. (1999) Anaerobic microbes: Oxygen detoxification without superoxide dismutase. *Science* **286**, 306–309
58. Sevcenco, A. M., Bevers, L. E., Pinkse, M. W. H., Krijger, G. C., Wolterbeek, H. T., Verhaert, P. D. E. M., Hagen, W. R., and Hagedoorn, P. L. (2010) Molybdenum incorporation in tungsten aldehyde oxidoreductase enzymes from *Pyrococcus furiosus*. *J. Bacteriol.* **192**, 4143–4152
59. Lipscomb, G. L., Stirrett, K., Schut, G. J., Yang, F., Jenney, F. E., Jr., Scott, R. A., Adams, M. W. W., and Westpheling, J. (2011) Natural competence in the hyperthermophilic archaeon *Pyrococcus furiosus* facilitates genetic manipulation: Construction of markerless deletions of genes encoding the two cytoplasmic hydrogenases. *Appl. Environ. Microbiol.* **77**, 2232–2238
60. Bridger, S. L., Clarkson, S. M., Stirrett, K., DeBarry, M. B., Lipscomb, G. L., Schut, G. J., Westpheling, J., Scott, R. A., and Adams, M. W. W. (2011) Deletion strains reveal metabolic roles for key elemental sulfur-responsive proteins in *Pyrococcus furiosus*. *J. Bacteriol.* **193**, 6498–6504